29. Cosmic Rays

Revised October 2017 by J.J. Beatty (Ohio State Univ.), J. Matthews (Louisiana State Univ.), and S.P. Wakely (Univ. of Chicago).

29.1. Primary spectra

The cosmic radiation incident at the top of the terrestrial atmosphere includes all stable charged particles and nuclei with lifetimes of order 10^6 years or longer. When discussing the astrophysical origin of cosmic rays, "primary" cosmic rays are those particles accelerated at astrophysical sources and "secondaries" are those particles produced in interaction of the primaries with interstellar gas†. Thus electrons, protons and helium, as well as carbon, oxygen, iron, and other nuclei synthesized in stars, are primaries. Nuclei such as lithium, beryllium, and boron (which are not abundant end-products of stellar nucleosynthesis) are secondaries. Antiprotons and positrons are also in large part secondary. Whether a small fraction of these particles may be primary is a question of current interest.

Apart from particles associated with solar flares, the cosmic radiation comes from outside the solar system. The incoming charged particles are "modulated" by the solar wind, the expanding magnetized plasma generated by the Sun, which decelerates and partially excludes the lower energy galactic cosmic rays from the inner solar system. There is a significant anticorrelation between solar activity (which has an alternating eleven-year cycle) and the intensity of the cosmic rays with rigidities below about 10 GV. In addition, the lower-energy cosmic rays are affected by the geomagnetic field, which they must penetrate to reach the top of the atmosphere. Thus the intensity of any component of the cosmic radiation in the GeV range depends both on the location and time.

There are four different ways to describe the spectra of the components of the cosmic radiation: (1) By particles per unit rigidity. Propagation (and probably also acceleration) through cosmic magnetic fields depends on gyroradius or *magnetic rigidity, R*, which is gyroradius multiplied by the magnetic field strength:

$$R = \frac{p\,c}{Z\,e} = r_{_L} B \ . \tag{29.1}$$

(2) By particles per energy-per-nucleon. Fragmentation of nuclei propagating through the interstellar gas depends on energy per nucleon, since that quantity is approximately conserved when a nucleus breaks up on interaction with the gas. (3) By nucleons per energy-per-nucleon. Production of secondary cosmic rays in the atmosphere depends on the intensity of nucleons per energy-per-nucleon, approximately independently of whether the incident nucleons are free protons or bound in nuclei. (4) By particles per energy-per-nucleus. Air shower experiments that use the atmosphere as a calorimeter generally measure a quantity that is related to total energy per particle.

† 'Primary' and 'secondary' are used in a different but analogous sense when discussing cosmic ray interactions in the atmosphere.

The units of differential intensity I are $[\mathrm{m}^{-2}\,\mathrm{s}^{-1}\mathrm{sr}^{-1}\mathcal{E}^{-1}]$, where $\mathcal{E}$ represents the units of one of the four variables listed above.

The intensity of primary nucleons in the energy range from several GeV to somewhat beyond 100 TeV is given approximately by

$$I_N(E) \;\approx\; 1.8 \times 10^4\,(E/1\ \mathrm{GeV})^{-\alpha}\ \frac{\mathrm{nucleons}}{\mathrm{m}^2\ \mathrm{s}\ \mathrm{sr}\ \mathrm{GeV}}\ , \tag{29.2}$$

where E is the energy-per-nucleon (including rest mass energy) and $\alpha\ (\equiv \gamma + 1) = 2.7$ is the differential spectral index of the cosmic-ray flux and γ is the integral spectral index. About 74% of the primary nucleons are free protons and about 70% of the rest are nucleons bound in helium nuclei. The fractions of the primary nuclei are nearly constant over this energy range (with a few interesting variations, e.g. [2]) . Fractions of both primary and secondary incident nuclei are listed in Table 29.1. Figure 29.1 shows the major components for kinetic energies greater than 0.22 GeV/nucleus. A useful compendium of experimental data for cosmic-ray nuclei and electrons is described in [1].

The composition and energy spectra of nuclei are typically interpreted in the context of propagation models, in which the sources of the primary cosmic radiation are located within the Galaxy [14]. The ratio of secondary to primary nuclei is observed to decrease with increasing energy, a fact often interpreted to mean that the lifetime of cosmic rays in the Galaxy decreases with energy. Measurements of radioactive "clock" isotopes in the low energy cosmic radiation are consistent with a lifetime in the Galaxy of about 15 Myr [15].

Table 29.1: Relative abundances F of cosmic-ray nuclei at 10.6 GeV/nucleon normalized to oxygen ($\equiv 1$) [10]. The oxygen flux at kinetic energy of 10.6 GeV/nucleon is 3.29×10^{-2} $(\mathrm{m}^2\ \mathrm{s\ sr\ GeV/nucleon})^{-1}$. Abundances of hydrogen and helium are from Refs. [3–5]. Note that one can not use these values to extend the cosmic-ray flux to high energy because the power law indices for each element may differ slightly.

Z	Element	F	Z	Element	F
1	H	550	13–14	Al-Si	0.19
2	He	34	15–16	P-S	0.03
3–5	Li-B	0.40	17–18	Cl-Ar	0.01
6–8	C-O	2.20	19–20	K-Ca	0.02
9–10	F-Ne	0.30	21–25	Sc-Mn	0.05
11–12	Na-Mg	0.22	26–28	Fe-Ni	0.12

Cosmic rays are nearly isotropic at most energies due to diffusive propagation in the galactic magnetic field. Milagro [16], IceCube [17], and the Tibet-III air shower

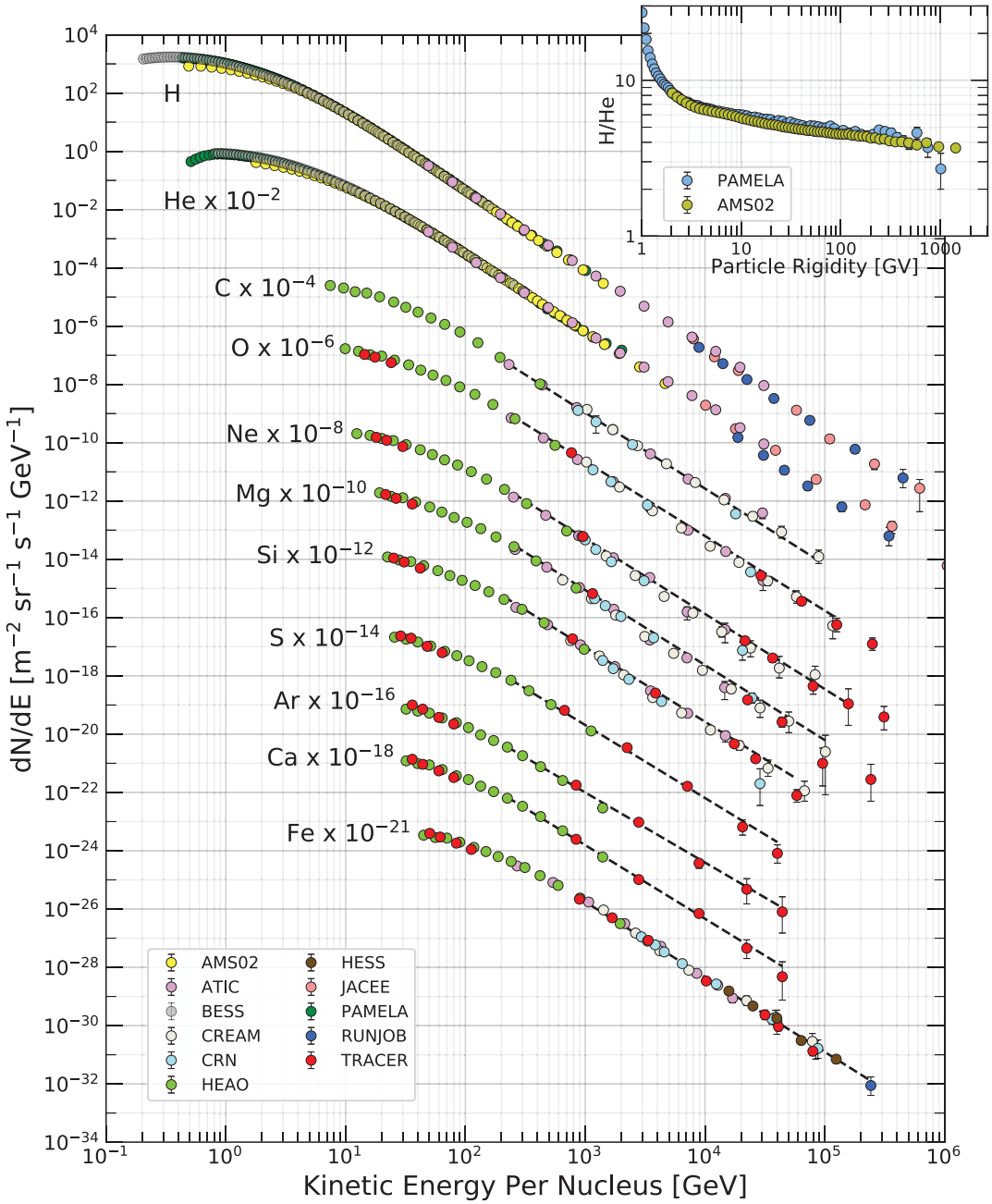

Figure 29.1: Fluxes of nuclei of the primary cosmic radiation in particles per energy-per-nucleus are plotted vs energy-per-nucleus using data from Refs. [2–13]. The inset shows the H/He ratio at constant rigidity [2,4].

array [18] have observed anisotropy at the level of about 10^{-3} for cosmic rays with energy of a few TeV, possibly due to the distribution of sources and the direction of local Galactic magnetic fields.

The spectrum of electrons and positrons incident at the top of the atmosphere is generally expected to steepen by one power of E at an energy of ∼5 GeV because of

strong radiative energy loss effects in the Galaxy. The ATIC experiment [19] measured a sharp excess of electrons over propagation model expectations, at energies of ∼300-800 GeV. The *Fermi*/LAT γ-ray observatory measured a not-entirely flat spectrum [20] without confirming the peak of the ATIC excess at ∼600 GeV. Measurements in the same energy range by AMS-02 also show no sharp features and are compatible with a single power law above 30.2 GeV [21]. The HESS imaging atmospheric Cherenkov array also measured the electron flux above ∼400 GeV, finding indications of a cutoff above ∼1 TeV [22], but no evidence for a pronounced peak below this.

The PAMELA [26] and AMS-02 [27,24] satellite experiments measured the positron to electron ratio to increase above 10 GeV instead of the expected decrease [28] at higher energy, confirming earlier hints seen by the HEAT balloon-borne experiment [30]. The structure in the electron spectrum, as well as the increase in the positron fraction, may be related to contributions from individual nearby sources (supernova remnants or pulsars) emerging above a background suppressed at high energy by synchrotron losses [31]. Other explanations have invoked propagation effects [32] or dark matter decay/annihilation processes (see, e.g., [29]) . The significant disagreement in the ratio below ∼10 GeV is attributable to differences in charge-sign dependent solar modulation effects present near Earth at the times of measurement.

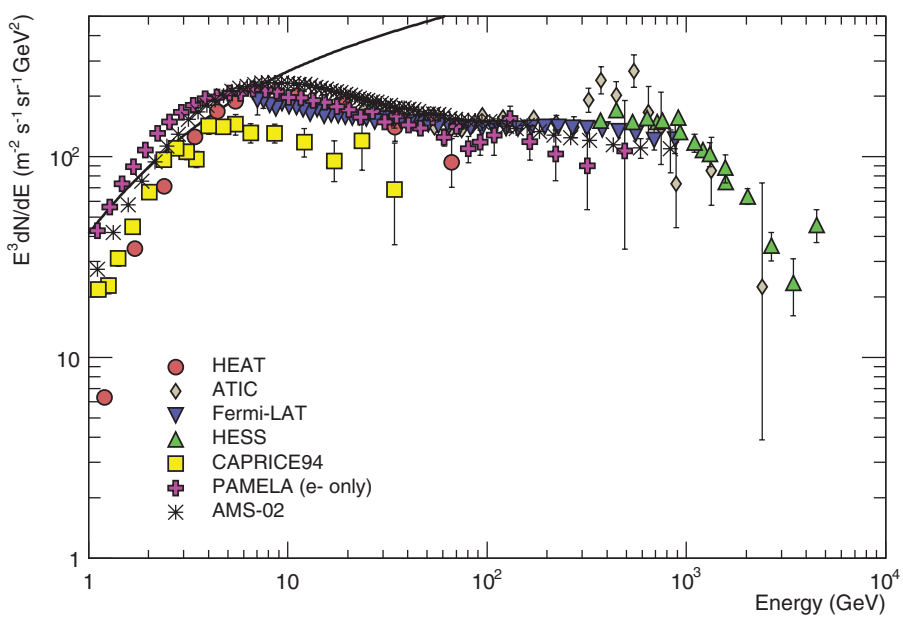

Figure 29.2: Differential spectrum of electrons plus positrons (except PAMELA data, which are electrons only) multiplied by E^3 [19–23,33,34]. The line shows the proton spectrum [25] multiplied by 0.01.

The ratio of antiprotons to protons is $\sim 2 \times 10^{-4}$ [35] at around 10–20 GeV, and there is clear evidence [36] for the kinematic suppression at lower energy that is the signature of secondary antiprotons. The $\overline{p}/p$ ratio also shows a strong dependence on the phase

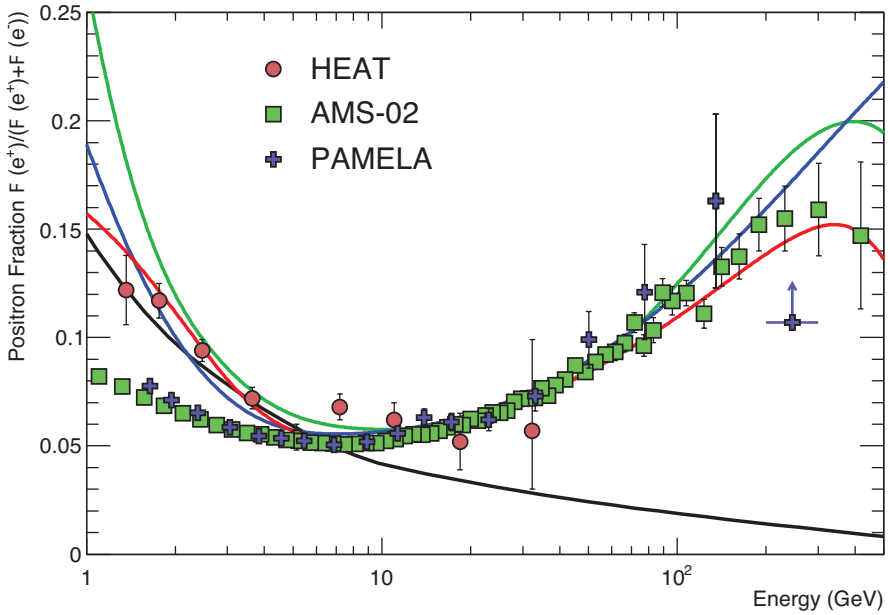

Figure 29.3: The positron fraction (ratio of the flux of e^+ to the total flux of e^+ and e^-) [26,24,30]. The heavy black line is a model of pure secondary production [28] and the three thin lines show three representative attempts to model the positron excess with different phenomena: green: dark matter decay [29]; blue: propagation physics [32]; red: production in pulsars [40]. The ratio below 10 GeV is dependent on the polarity of the solar magnetic field.

and polarity of the solar cycle [37] in the opposite sense to that of the positron fraction. There is at this time no evidence for a significant primary component of antiprotons. No antihelium or antideuteron has been found in the cosmic radiation. The best measured upper limit on the ratio antihelium/helium is currently approximately 1×10^{-7} [38] The upper limit on the flux of antideuterons around 1 GeV/nucleon is approximately $2 \times 10^{-4}\,(\mathrm{m^2\ s\ sr\ GeV/nucleon})^{-1}$ [39].

29.2. Cosmic rays in the atmosphere

Figure 29.4 shows the vertical fluxes of the major cosmic-ray components in the atmosphere in the energy region where the particles are most numerous (except for electrons, which are most numerous near their critical energy, which is about 81 MeV in air). Except for protons and electrons near the top of the atmosphere, all particles are produced in interactions of the primary‡ cosmic rays in the air. Muons and neutrinos are products of the decay chain of charged mesons, while electrons and photons originate in decays of neutral mesons.

‡ When discussing cosmic rays in the atmosphere, 'primary' is used to denote the original particle and 'secondary' to denote the particles produced in interactions.

Most measurements are made at ground level or near the top of the atmosphere, but there are also measurements of muons and electrons from airplanes and balloons. Fig. 29.4 includes recent measurements of negative muons [41–45]. Since $\mu^+(\mu^-)$ are produced in association with $\nu_\mu(\overline{\nu}_\mu)$, the measurement of muons near the maximum of the intensity curve for the parent pions serves to calibrate the atmospheric ν_μ beam [46]. Because muons typically lose almost 2 GeV in passing through the atmosphere, the comparison near the production altitude is important for the sub-GeV range of $\nu_\mu(\overline{\nu}_\mu)$ energies.

The flux of cosmic rays through the atmosphere is described by a set of coupled cascade equations with boundary conditions at the top of the atmosphere to match the primary spectrum. Numerical or Monte Carlo calculations are needed to account accurately for decay and energy-loss processes, and for the energy-dependences of the cross sections and of the primary spectral index γ. Approximate analytic solutions are, however, useful in limited regions of energy [47,48]. For example, the vertical intensity of charged pions with energy $E_\pi \ll \epsilon_\pi = 115$ GeV is

$$I_\pi(E_\pi, X) \approx \frac{Z_{N\pi}}{\lambda_N} I_N(E_\pi, 0)\, e^{-X/\Lambda} \frac{X\, E_\pi}{\epsilon_\pi} , \tag{29.3}$$

where Λ is the characteristic length for exponential attenuation of the parent nucleon flux in the atmosphere. This expression has a maximum at $X = \Lambda \approx 121 \pm 4$ g cm^{-2} [49], which corresponds to an altitude of 15 kilometers. The quantity $Z_{N\pi}$ is the spectrum-weighted moment of the inclusive distribution of charged pions in interactions of nucleons with nuclei of the atmosphere. The intensity of low-energy pions is much less than that of nucleons because $Z_{N\pi} \approx 0.079$ is small and because most pions with energy much less than the critical energy ϵ_π decay rather than interact.

29.3. Cosmic rays at the surface

29.3.1. ***Muons*** : Muons are the most numerous charged particles at sea level (see Fig. 29.4). Most muons are produced high in the atmosphere (typically 15 km) and lose about 2 GeV to ionization before reaching the ground. Their energy and angular distribution reflect a convolution of the production spectrum, energy loss in the atmosphere, and decay. For example, 2.4 GeV muons have a decay length of 15 km, which is reduced to 8.7 km by energy loss. The mean energy of muons at the ground is ≈ 4 GeV. The energy spectrum is almost flat below 1 GeV, steepens gradually to reflect the primary spectrum in the 10–100 GeV range, and steepens further at higher energies because pions with $E_\pi > \epsilon_\pi$ tend to interact in the atmosphere before they decay. Asymptotically ($E_\mu \gg 1$ TeV), the energy spectrum of atmospheric muons is one power steeper than the primary spectrum. The integral intensity of vertical muons above 1 GeV/c at sea level is ≈ 70 m^{-2}s^{-1}sr^{-1} [50,51], with recent measurements [52–54] favoring a lower normalization by 10-15%. Experimentalists are familiar with this number in the form $I \approx 1$ cm^{-2} min^{-1} for horizontal detectors. The overall angular distribution of muons at the ground as a funxtion of zenith angle θ is $\propto \cos^2\theta$, which is characteristic of muons with $E_\mu \sim 3$ GeV. At lower energy the angular distribution becomes increasingly steep, while at higher energy it flattens, approaching a $\sec\theta$ distribution for $E_\mu \gg \epsilon_\pi$ and $\theta < 70^\circ$.

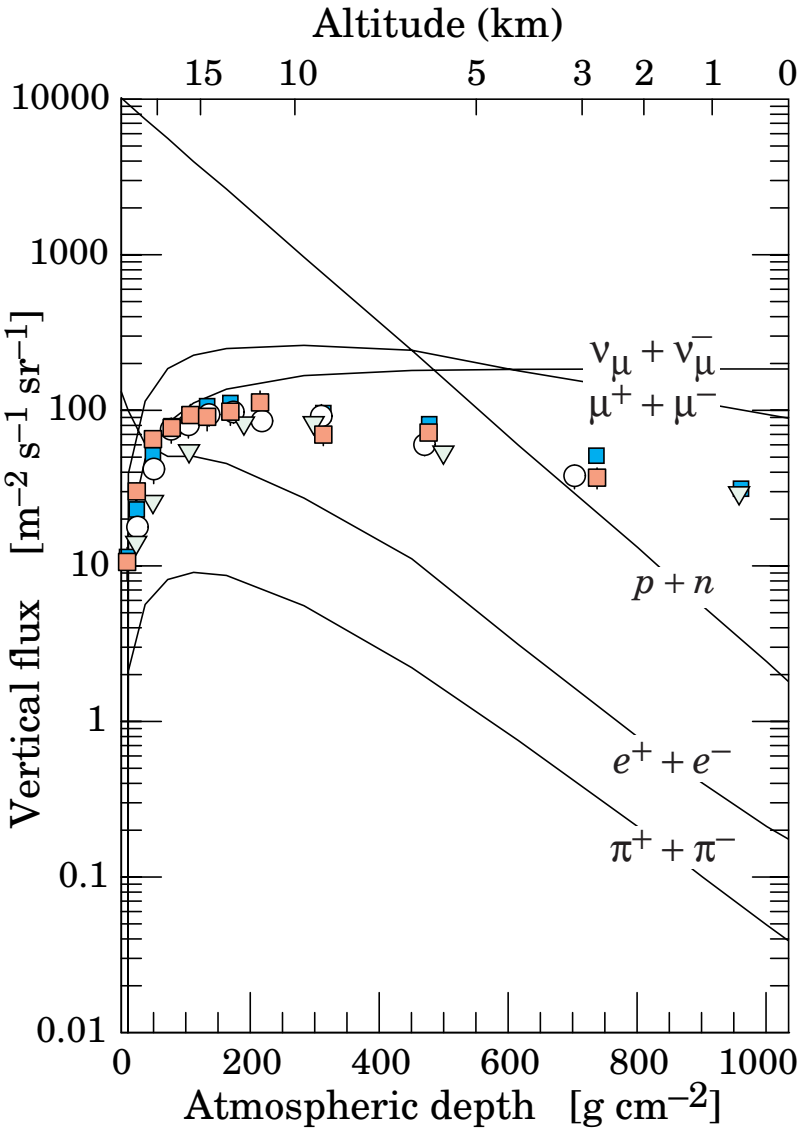

Figure 29.4: Vertical fluxes of cosmic rays in the atmosphere with $E > 1$ GeV estimated from the nucleon flux of Eq. (29.2). The points show measurements of negative muons with $E_\mu > 1$ GeV [41–45].

Figure 29.5 shows the muon energy spectrum at sea level for two angles. At large angles low energy muons decay before reaching the surface and high energy pions decay before they interact, thus the average muon energy increases. An approximate extrapolation formula valid when muon decay is negligible ($E_\mu > 100/\cos\theta$ GeV) and the curvature of the Earth can be neglected ($\theta < 70^\circ$) is

$$\frac{dN_\mu}{dE_\mu d\Omega} \approx \frac{0.14\, E_\mu^{-2.7}}{\text{cm}^2 \text{ s sr GeV}}$$

$$\times \left\{ \frac{1}{1 + \dfrac{1.1 E_\mu \cos\theta}{115\,\mathrm{GeV}}} + \frac{0.054}{1 + \dfrac{1.1 E_\mu \cos\theta}{850\,\mathrm{GeV}}} \right\} , \tag{29.4}$$

where the two terms give the contribution of pions and charged kaons. Eq. (29.4) neglects a small contribution from charm and heavier flavors which is negligible except at very high energy [55].

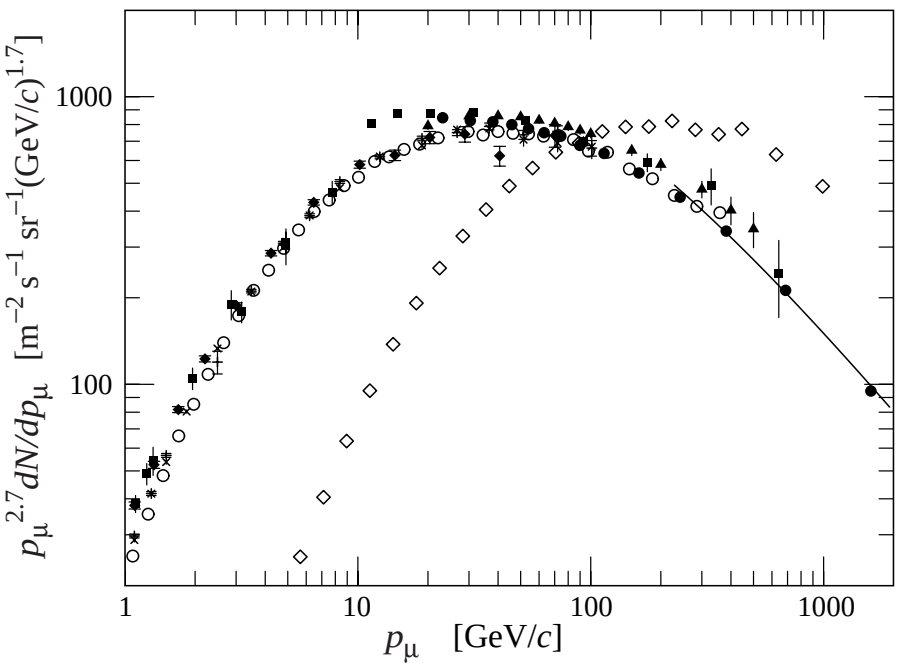

Figure 29.5: Spectrum of muons at $\theta = 0°$ (⧫ [50], ■ [56], ▼ [57], ▲ [58], ×, + [52], ○ [53], and • [54] and $\theta = 75°$ ◇ [59]) . The line plots the result from Eq. (29.4) for vertical showers.

The muon charge ratio reflects the excess of π^+ over π^- and K^+ over K^- in the forward fragmentation region of proton initiated interactions together with the fact that there are more free and bound protons than free and bound neutrons in the primary spectrum. The increase with energy of μ^+/μ^- shown in Fig. 29.6 reflects the increasing importance of kaons in the TeV range [60] and indicates a significant contribution of associated production by cosmic-ray protons ($p \to \Lambda + K^+$). The same process is even more important for atmospheric neutrinos at high energy.

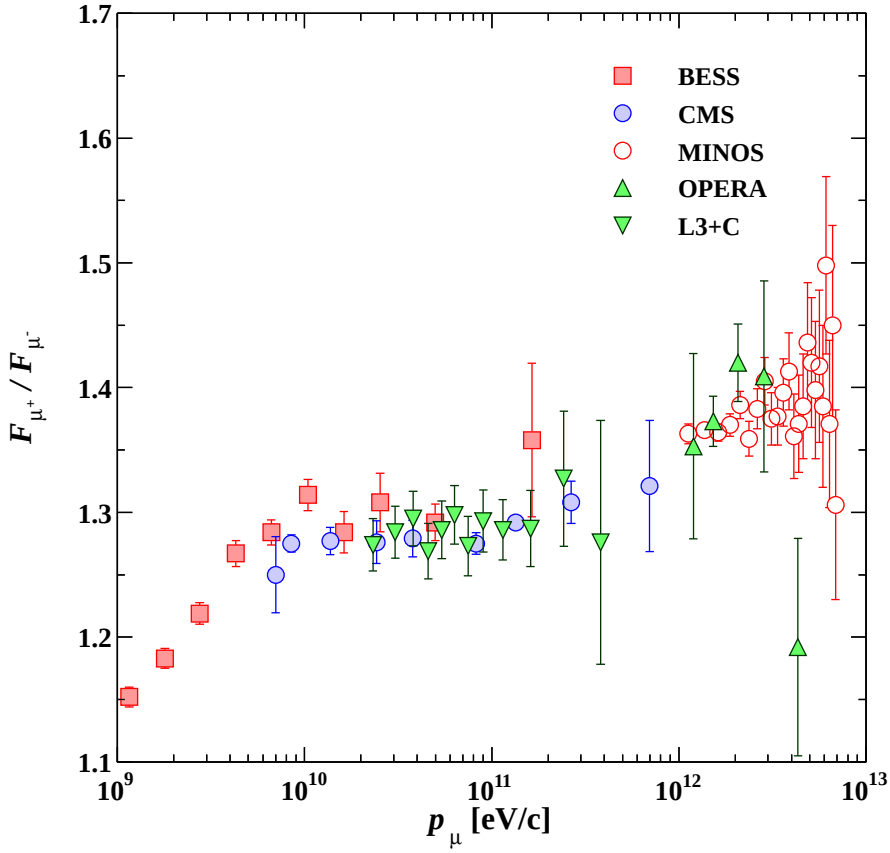

Figure 29.6: Muon charge ratio as a function of the muon momentum from Refs. [53,54,60,65,66].

29.3.2. ***Electromagnetic component*** : At the ground, this component consists of electrons, positrons, and photons primarily from cascades initiated by decay of neutral and charged mesons. Muon decay is the dominant source of low-energy electrons at sea level. Decay of neutral pions is more important at high altitude or when the energy threshold is high. Knock-on electrons also make a small contribution at low energy [61]. The integral vertical intensity of electrons plus positrons is very approximately 30, 6, and 0.2 $\mathrm{m^{-2}s^{-1}sr^{-1}}$ above 10, 100, and 1000 MeV respectively [51,62], but the exact numbers depend sensitively on altitude, and the angular dependence is complex because of the different altitude dependence of the different sources of electrons [61–63]. The ratio of photons to electrons plus positrons is approximately 1.3 above 1 GeV and 1.7 below the critical energy [63].

29.3.3. ***Protons*** : Nucleons above 1 GeV/c at ground level are degraded remnants of the primary cosmic radiation. The intensity is approximately $I_N(E,0) \times \exp(-X/\cos\theta\Lambda)$ for $\theta < 70°$. At sea level, about 1/3 of the nucleons in the vertical direction are neutrons (up from $\approx 10\%$ at the top of the atmosphere as the n/p ratio approaches equilibrium). The integral intensity of vertical protons above 1 GeV/c at sea level is ≈ 0.9 m^{-2}s^{-1}sr^{-1} [51,64].

29.4. Cosmic rays underground

Only muons and neutrinos penetrate to significant depths underground. The muons produce tertiary fluxes of photons, electrons, and hadrons.

29.4.1. ***Muons*** : As discussed in Section 33.6 of this *Review*, muons lose energy by ionization and by radiative processes: bremsstrahlung, direct production of e^+e^- pairs, and photonuclear interactions. The total muon energy loss may be expressed as a function of the amount of matter traversed as

$$-\frac{dE_\mu}{dX} = a + b\,E_\mu \ , \tag{29.5}$$

where a is the ionization loss and b is the fractional energy loss by the three radiation processes. Both are slowly varying functions of energy. The quantity $\epsilon \equiv a/b$ (≈ 500 GeV in standard rock) defines a critical energy below which continuous ionization loss is more important than radiative losses. Table 29.2 shows a and b values for standard rock, and b for ice, as a function of muon energy. The second column of Table 29.2 shows the muon range in standard rock ($A = 22$, $Z = 11$, $\rho = 2.65$ g cm^{-3}). These parameters are quite sensitive to the chemical composition of the rock, which must be evaluated for each location.

Table 29.2: Average muon range R and energy loss parameters a and b calculated for standard rock [67] and the total energy loss parameter b for ice. Range is given in km-water-equivalent, or 10^5 g cm^{-2}.

E_μ	R	a	$b_{\rm brems}$	$b_{\rm pair}$	$b_{\rm nucl}$	$\sum b_i$	$\sum b$(ice)
GeV	km.w.e.	MeV g^{-1} cm^2	—	10^{-6} g^{-1} cm^2		—	
10	0.05	2.17	0.70	0.70	0.50	1.90	1.66
100	0.41	2.44	1.10	1.53	0.41	3.04	2.51
1000	2.45	2.68	1.44	2.07	0.41	3.92	3.17
10000	6.09	2.93	1.62	2.27	0.46	4.35	3.78

The intensity of muons underground can be estimated from the muon intensity in the atmosphere and their rate of energy loss. To the extent that the mild energy dependence

of a and b can be neglected, Eq. (29.5) can be integrated to provide the following relation between the energy $E_{\mu,0}$ of a muon at production in the atmosphere and its average energy E_μ after traversing a thickness X of rock (or ice or water):

$$E_{\mu,0} \;=\; (E_\mu + \epsilon)\, e^{bX} \;-\; \epsilon \;. \tag{29.6}$$

Especially at high energy, however, fluctuations are important and an accurate calculation requires a simulation that accounts for stochastic energy-loss processes [68].

There are two depth regimes for which Eq. (29.6) can be simplified. For $X \ll b^{-1} \approx 2.5$ km water equivalent, $E_{\mu,0} \approx E_\mu(X) + aX$, while for $X \gg b^{-1}$ $E_{\mu,0} \approx (\epsilon + E_\mu(X)) \exp(bX)$. Thus at shallow depths the differential muon energy spectrum is approximately constant for $E_\mu < aX$ and steepens to reflect the surface muon spectrum for $E_\mu > aX$, whereas for $X > 2.5$ km.w.e. the differential spectrum underground is again constant for small muon energies but steepens to reflect the surface muon spectrum for $E_\mu > \epsilon \approx 0.5$ TeV. In the deep regime the shape is independent of depth although the intensity decreases exponentially with depth. In general the muon spectrum at slant depth X is

$$\frac{dN_\mu(X)}{dE_\mu} \;=\; \frac{dN_\mu}{dE_{\mu,0}}\,\frac{dE_{\mu,0}}{dE_\mu} \;=\; \frac{dN_\mu}{dE_{\mu,0}}\, e^{bX} \;, \tag{29.7}$$

where $E_{\mu,0}$ is the solution of Eq. (29.6) in the approximation neglecting fluctuations.

Fig. 29.7 shows the vertical muon intensity versus depth. In constructing this "depth-intensity curve," each group has taken account of the angular distribution of the muons in the atmosphere, the map of the overburden at each detector, and the properties of the local medium in connecting measurements at various slant depths and zenith angles to the vertical intensity. Use of data from a range of angles allows a fixed detector to cover a wide range of depths. The flat portion of the curve is due to muons produced locally by charged-current interactions of ν_μ. The inset shows the vertical intensity curve for water and ice published in Refs. [70–73]. It is not as steep as the one for rock because of the lower muon energy loss in water.

29.4.2. *Neutrinos* :

Because neutrinos have small interaction cross sections, measurements of atmospheric neutrinos require a deep detector to avoid backgrounds. There are two types of measurements: contained (or semi-contained) events, in which the vertex is determined to originate inside the detector, and neutrino-induced muons. The latter are muons that enter the detector from zenith angles so large (*e.g.*, nearly horizontal or upward) that they cannot be muons produced in the atmosphere. In neither case is the neutrino flux measured directly. What is measured is a convolution of the neutrino flux and cross section with the properties of the detector (which includes the surrounding medium in the case of entering muons).

Contained and semi-contained events reflect neutrinos in the sub-GeV to multi-GeV region where the product of increasing cross section and decreasing flux is maximum. In the GeV region the neutrino flux and its angular distribution depend on the geomagnetic

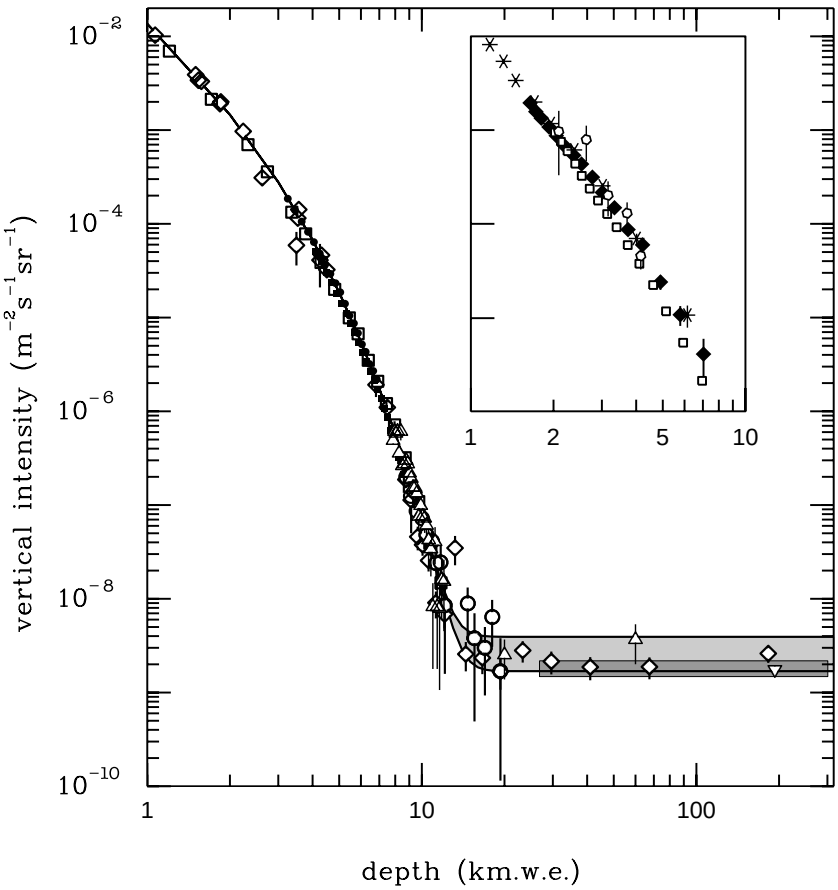

Figure 29.7: Vertical muon intensity vs depth (1 km.w.e. = 10^5 g cm^{-2} of standard rock). The experimental data are from: ◊: the compilations of Crouch [69], □: Baksan [75], ○: LVD [76], •: MACRO [77], ■: Frejus [78], and △: SNO [79]. The shaded area at large depths represents neutrino-induced muons of energy above 2 GeV. The upper line is for horizontal neutrino-induced muons, the lower one for vertically upward muons. Darker shading shows the muon flux measured by the SuperKamiokande experiment. The inset shows the vertical intensity curve for water and ice published in Refs. [70–73]. Additional data extending to slant depths of 13 km are available in [74].

location of the detector and, to a lesser extent, on the phase of the solar cycle. Naively, we expect $\nu_\mu/\nu_e = 2$ from counting neutrinos of the two flavors coming from the chain of pion and muon decays. Contrary to expectation, however, the numbers of the two classes of events are similar rather than different by a factor of two. This is now understood to be a consequence of neutrino flavor oscillations [82]. (See the article on neutrino properties in this *Review*.)

Two well-understood properties of atmospheric cosmic rays provide a standard for comparison of the measurements of atmospheric neutrinos to expectation. These are the "sec θ effect" and the "east-west effect" [81]. The former refers originally to the enhancement of the flux of > 10 GeV muons (and neutrinos) at large zenith angles because

the parent pions propagate more in the low density upper atmosphere where decay is enhanced relative to interaction. For neutrinos from muon decay, the enhancement near the horizontal becomes important for $E_\nu > 1$ GeV and arises mainly from the increased pathlength through the atmosphere for muon decay in flight. Fig. 14.11 from Ref. 80 shows a comparison between measurement and expectation for the zenith angle dependence of multi-GeV electron-like (mostly ν_e) and muon-like (mostly ν_μ) events separately. The ν_e show an enhancement near the horizontal and approximate equality for nearly upward ($\cos\theta \approx -1$) and nearly downward ($\cos\theta \approx 1$) events. There is, however, a very significant deficit of upward ($\cos\theta < 0$) ν_μ events, which have long pathlengths comparable to the radius of the Earth. This feature is the principal signature for atmospheric neutrino oscillations [82].

Muons that enter the detector from outside after production in charged-current interactions of neutrinos naturally reflect a higher energy portion of the neutrino spectrum than contained events because the muon range increases with energy as well as the cross section. The relevant energy range is $\sim 10 < E_\nu < 1000$ GeV, depending somewhat on angle. Neutrinos in this energy range show a $\sec\theta$ effect similar to muons (see Eq. (29.4)). This causes the flux of horizontal neutrino-induced muons to be approximately a factor two higher than the vertically upward flux. The upper and lower edges of the horizontal shaded region in Fig. 29.7 correspond to horizontal and vertical intensities of neutrino-induced muons. Table 29.3 gives the measured fluxes of upward-moving neutrino-induced muons averaged over the lower hemisphere. Generally the definition of minimum muon energy depends on where it passes through the detector. The tabulated effective minimum energy estimates the average over various accepted trajectories.

Table 29.3: Measured fluxes (10^{-9} m^{-2} s^{-1} sr^{-1}) of neutrino-induced muons as a function of the effective minimum muon energy E_μ.

$E_\mu >$	1 GeV	1 GeV	1 GeV	2 GeV	3 GeV	3 GeV
Ref.	CWI [83]	Baksan [84]	MACRO [85]	IMB [86]	Kam [87]	SuperK [88]
F_μ	2.17±0.21	2.77±0.17	2.29 ± 0.15	2.26±0.11	1.94±0.12	1.74±0.07

29.5. Air showers

So far we have discussed inclusive or uncorrelated fluxes of various components of the cosmic radiation. An air shower is caused by a single cosmic ray with energy high enough for its cascade to be detectable at the ground. The shower has a hadronic core, which acts as a collimated source of electromagnetic subshowers, generated mostly from $\pi^0 \to \gamma\,\gamma$ decays. The resulting electrons and positrons are the most numerous charged particles in the shower. The number of muons, produced by decays of charged mesons, is an order of magnitude lower. Air showers spread over a large area on the ground, and arrays of detectors operated for long times are useful for studying cosmic rays with primary energy $E_0 > 100$ TeV, where the low flux makes measurements with small detectors in balloons and satellites difficult.

Greisen [89] gives the following approximate expressions for the numbers and lateral distributions of particles in showers at ground level. The total number of muons N_μ with energies above 1 GeV is

$$N_\mu(> 1\ \mathrm{GeV}) \;\approx\; 0.95 \times 10^5 \left(N_e/10^6\right)^{3/4} \;, \tag{29.8}$$

where N_e is the total number of charged particles in the shower (not just $e^\pm$). The number of muons per square meter, ρ_μ, as a function of the lateral distance r (in meters) from the center of the shower is

$$\rho_\mu = \frac{1.25\,N_\mu}{2\pi\,\Gamma(1.25)} \left(\frac{1}{320}\right)^{1.25} r^{-0.75} \left(1 + \frac{r}{320}\right)^{-2.5} \;, \tag{29.9}$$

where Γ is the gamma function. The number density of charged particles is

$$\rho_e = C_1(s, d, C_2)\, x^{(s-2)}(1+x)^{(s-4.5)}(1 + C_2 x^d) \;. \tag{29.10}$$

Here s, d, and C_2 are parameters in terms of which the overall normalization constant $C_1(s, d, C_2)$ is given by

$$C_1(s, d, C_2) = \frac{N_e}{2\pi r_1^2}\,[\,B(s, 4.5 - 2s) + C_2\,B(s + d,\, 4.5 - d - 2s)]^{-1} \;, \tag{29.11}$$

where $B(m, n)$ is the beta function. The values of the parameters depend on shower size (N_e), depth in the atmosphere, identity of the primary nucleus, etc. For showers with $N_e \approx 10^6$ at sea level, Greisen uses $s = 1.25$, $d = 1$, and $C_2 = 0.088$. Finally, x is r/r_1, where r_1 is the Molière radius, which depends on the density of the atmosphere and hence on the altitude at which showers are detected. At sea level $r_1 \approx 78$ m. It increases with altitude as the air density decreases. (See the section on electromagnetic cascades in the article on the passage of particles through matter in this *Review*).

The lateral spread of a shower is determined largely by Coulomb scattering of the many low-energy electrons and is characterized by the Molière radius. The lateral spread

of the muons (ρ_μ) is larger and depends on the transverse momenta of the muons at production as well as multiple scattering.

There are large fluctuations in development from shower to shower, even for showers of the same energy and primary mass—especially for small showers, which are usually well past maximum development when observed at the ground. Thus the shower size N_e and primary energy E_0 are only related in an average sense, and even this relation depends on depth in the atmosphere. One estimate of the relation is [96]

$$E_0 \sim 3.9 \times 10^6 \text{ GeV } (N_e/10^6)^{0.9} \tag{29.12}$$

for vertical showers with $10^{14} < E < 10^{17}$ eV at 920 g cm^{-2} (965 m above sea level). As E_0 increases the shower maximum (on average) moves down into the atmosphere and the relation between N_e and E_0 changes. Moreover, because of fluctuations, N_e as a function of E_0 is not correctly obtained by inverting Eq. (29.12). At the maximum of shower development, there are approximately 2/3 particles per GeV of primary energy.

There are three common types of air shower detectors: shower arrays that measure a ground parameter related to shower size N_e and muon number N_μ as well as the lateral distribution on the ground, Cherenkov detectors that detect the Cherenkov radiation emitted by the charged particles of the shower, and fluorescence detectors that study the nitrogen fluorescence excited by the charged particles in the shower. The fluorescence light is emitted isotropically so the showers can be observed from the side. Detection of radiofrequency emission from showers via geosynchrotron and Askaryan mechanisms has also been successfully employed in recent experiments. Detailed simulations and cross-calibrations between different types of detectors are necessary to establish the primary energy spectrum from air-shower experiments.

Figure 29.8 shows the "all-particle" spectrum. The differential energy spectrum has been multiplied by $E^{2.6}$ in order to display the features of the steep spectrum that are otherwise difficult to discern. The steepening that occurs between 10^{15} and 10^{16} eV is known as the *knee* of the spectrum. The feature around $10^{18.5}$ eV is called the *ankle* of the spectrum.

Measurements of flux with air shower experiments in the knee region differ by as much as a factor of two, indicative of systematic uncertainties in interpretation of the data. (For a review see Ref. 90.) In establishing the spectrum shown in Fig. 29.8, efforts have been made to minimize the dependence of the analysis on the primary composition. Ref. 99 uses an unfolding procedure to obtain the spectra of the individual components, giving a result for the all-particle spectrum between 10^{15} and 10^{17} eV that lies toward the upper range of the data shown in Fig. 29.8. In the energy range above 10^{17} eV, the fluorescence technique [107] is particularly useful because it can establish the primary energy in a model-independent way by observing most of the longitudinal development of each shower, from which E_0 is obtained by integrating the energy deposition in the atmosphere. The result, however, depends strongly on the light absorption in the atmosphere and the calculation of the detector's aperture.

Assuming the cosmic-ray spectrum below 10^{18} eV is of galactic origin, the *knee* could reflect the fact that most cosmic accelerators in the Galaxy have reached their maximum

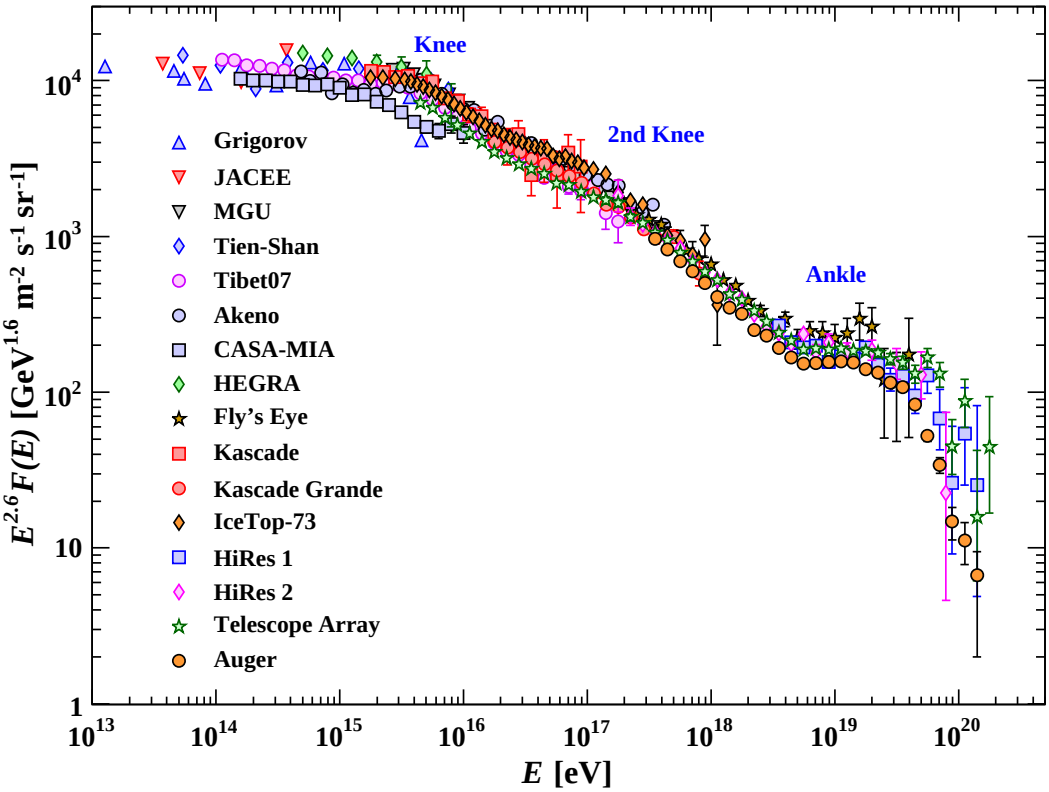

Figure 29.8: The all-particle spectrum as a function of E (energy-per-nucleus) from air shower measurements [91–106].

energy. Some types of expanding supernova remnants, for example, are estimated not to be able to accelerate protons above energies in the range of 10^{15} eV. Effects of propagation and confinement in the Galaxy [111] also need to be considered. A discussion of models of the knee may be found in Ref. 112. The Kascade-Grande experiment [101] has reported observation of a second steepening of the spectrum near 8×10^{16} eV, with evidence that this structure is accompanied a transition to heavy primaries.

Concerning the ankle, one possibility is that it is the result of a higher energy population of particles overtaking a lower energy population, for example an extragalactic flux beginning to dominate over the galactic flux (e.g. Ref. 107). Another possibility is that the dip structure in the region of the ankle is due to $p\gamma \to e^+ + e^-$ energy losses of extragalactic protons on the 2.7 K cosmic microwave radiation (CMB) [114]. This dip structure has been cited as a robust signature of both the protonic and extragalactic nature of the highest energy cosmic rays [113]. If this interpretation is correct, then the galactic cosmic rays do not contribute significantly to the flux above 10^{18} eV.

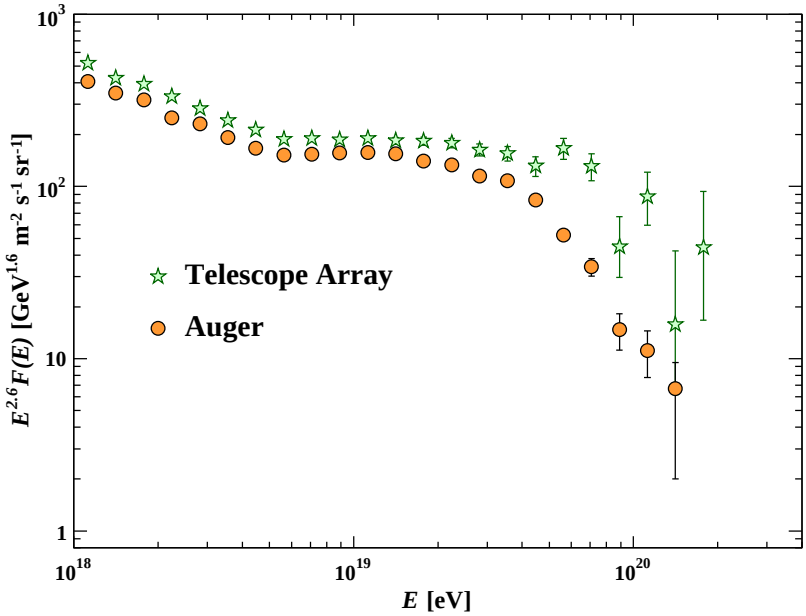

Figure 29.9: Expanded view of the highest energy portion of the cosmic-ray spectrum from data of the Telescope Array [105], and the Pierre Auger Observatory [106].

The energy-dependence of the composition from the knee through the ankle is useful in discriminating between these two viewpoints, since a heavy composition above 10^{18} eV is inconsistent with the formation of the ankle by pair production losses on the CMB. The TA and Auger experiments, however, have shown somewhat different interpretations of data on the depth of shower maximum X_{max}, a quantity that correlates strongly with $ln(E/A)$ and with the interaction cross section of the primary particle. The Telescope Array (TA) collaboration [115] has interpreted their data as implying a light primary composition (mainly p and He) of ultrahigh-energy cosmic-rays (UHECR) from 1.3×10^{18} to 4×10^{19} eV. The Pierre Auger collaboration [116], using post-LHC hadronic interaction models, reports a composition becoming light up to 2×10^{18} eV but then becoming heavier above that energy, with the mean mass intermediate between protons and iron at 3×10^{19} eV. Auger and TA have also conducted a thorough joint analysis [117] and state that, at the current level of statistics and understanding of systematics, both data sets are compatible with being drawn from the same parent distribution, and that the TA data is compatible both with a protonic compsition below 10^{19} eV and with the mixed compostion above 10^{19} eV as reported by Auger.

If the cosmic-ray flux at the highest energies is cosmological in origin, there should be a rapid steepening of the spectrum (called the GZK feature) around 5×10^{19} eV, resulting from the onset of inelastic interactions of UHE cosmic rays with the cosmic microwave background [118,119]. Photo-dissociation of heavy nuclei in the mixed composition

model [120] would have a similar effect. UHECR experiments have detected events of energy above 10^{20} eV [107–108]. The HiRes fluorescence experiment [103,131] detected evidence of the GZK suppression, and the Auger observatory [104–106] has also presented spectra showing this suppression based on surface detector measurements calibrated against fluorescence detectors using events detected in hybrid mode, i.e. with both the surface and the fluorescence detectors. The Telescope Array (TA) [105] has also presented a spectrum showing this suppression. The differential energy spectra measured by the TA and by Auger agree within systematic errors below 10^{19} eV (Fig. 29.9). At higher energies, TA observes more cosmic rays than would be expected if the spectral shape were the same as that seen by Auger. TA has also reported a 'hot spot' in the Northern Hemisphere at energies above 5.5×10^{19} eV of radius $\sim 20°$ with a post-trials statistical significance of this excess with respect to an isotropic distribution of 3.4σ [109]. Auger has reported the observation of a dipole of amplitude $6.5^{+1.3}_{-0.9}\%$ with a significance of 5.2σ for cosmic rays with energies above 8×10^{18} eV. The direction of the dipole indicates an extragalactic origin for these particles [110].

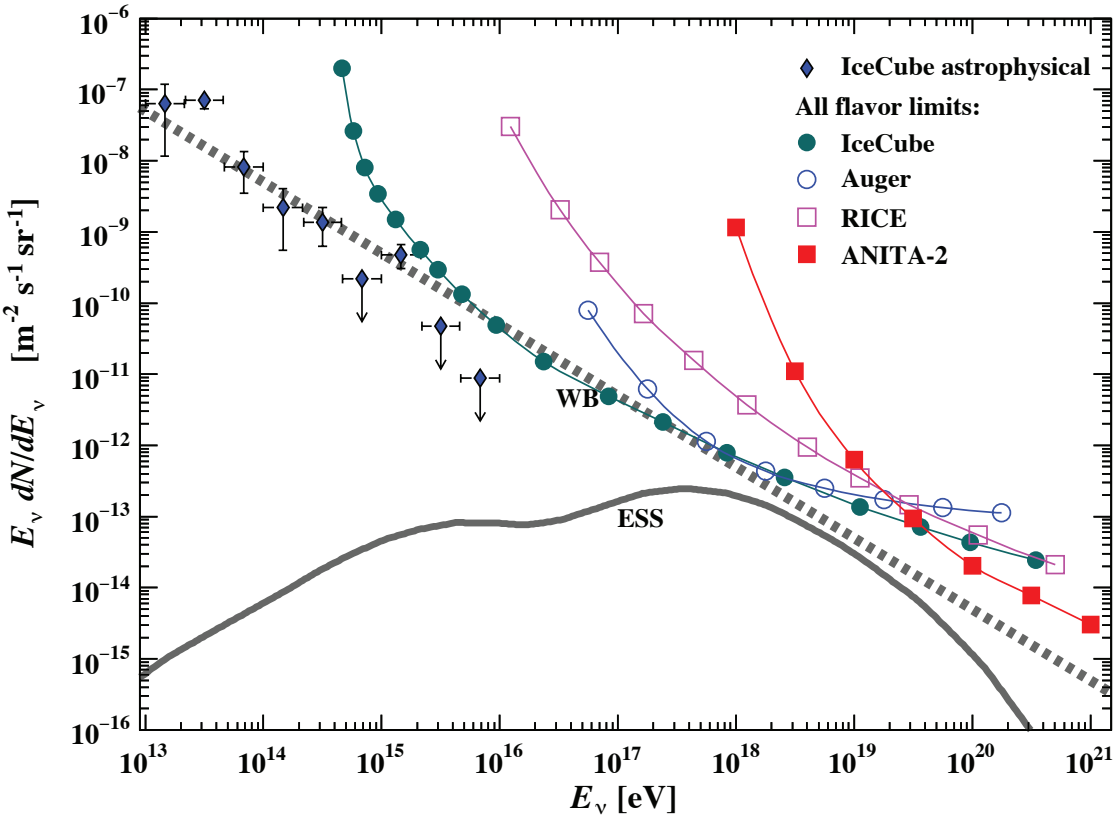

Figure 29.10: The best-fit IceCube astrophysical all-flavor neutrino flux [123]. Also shown are differential limits on the flux of cosmogenic neutrinos set by four experiments [125–128]. The curves show the Waxman-Bahcall benchmark flux (WB, [130]) and a representative midrange model for the expected flux of cosmogenic neutrinos (ESS, [129]) . The expected flux is uncertain by over an order of magnitude in either direction.

Neutrinos are expected to be produced in hadronic interactions in a variety of astrophysical objects. IceCube has reported a population of astrophysical neutrino events extending from tens of TeV up to several PeV [121–123].

There is also expected to be a neutrino flux produced in cosmic ray GZK interactions. One half of the energy that UHECR protons lose in photoproduction interactions that cause the GZK effects ends up in neutrinos [124]. Measuring this *cosmogenic* neutrino flux above 10^{18} eV would help resolve the UHECR uncertainties mentioned above. The magnitude of this flux depends strongly on the cosmic-ray spectrum at acceleration, the cosmic-ray composition, and the cosmological evolution of the cosmic-ray sources. In the case that UHECR have mixed composition only the proton fraction would produce cosmogenic neutrinos. Heavy nuclei propagation produces mostly $\bar{\nu}_e$ at lower energy from neutron decay.

The expected rate of cosmogenic neutrinos is lower than current limits obtained by IceCube [125], the Auger observatory [126], RICE [127], and ANITA-2 [128], which are shown in Fig. 29.10 together with a model for cosmogenic neutrino production [129] and the Waxman-Bahcall benchmark flux of neutrinos produced in cosmic ray sources [130]. At production, the dominant component of neutrinos comes from $\pi^{\pm}$ decays and has flavor content $\nu_e : \nu_\mu : \nu_\tau = 1 : 2 : 0$. After oscillations, the arriving cosmogenic neutrinos are expected to be an equal mixture of all three flavors. The sensitivity of each experiment depends on neutrino flavor. IceCube, RICE, and ANITA are sensitive to all three flavors, and the sensitivity to different flavors is energy dependent. The limit of Auger is only for ν_τ and $\bar{\nu}_\tau$ which should be about 1/3 of the total neutrino flux after oscillations, so this limit is plotted multiplied by a factor of three for comparison with the other limits and with the theoretical estimates.

References:

1. D. Maurin *et al.*, Astron. & Astrophys. **569**, A32 (2014).
2. O. Adriani *et al.* (PAMELA Collab.), Science **332**, 69 (2011).
3. M. Aguilar *et al.* (AMS02 Collab.), Phys. Rev. Lett. **114**, 171103 (2015).
4. M. Aguilar *et al.* (AMS02 Collab.), Phys. Rev. Lett. **115**, 211101 (2015).
5. K. Abe *et al.* (BESS Collab.), Astrophys. J. **822**, 65 (2016).
6. K. Asakimori *et al.* (JACEE Collab.), Astrophys. J. **502**, 278 (1998).
7. A.D. Panov *et al.*(ATIC Collab.), Bull. Russian Acad. of Science, Physics, **73**, 564 (2009).
8. V.A. Derbina *et al.*(RUNJOB Collab.), Astrophys. J. **628**, L41 (2005).
9. H.S. Ahn, *et al.* (CREAM Collab.), Astrophys. J. **707**, 593 (2009).
10. J.J. Engelmann *et al.*(HEAO3-C2 Collab.), Astron. & Astrophys. **233**, 96 (1990).
11. D. Müller *et al.*(CRN Collab.), Astrophys. J. **374**, 356 (1991).
12. M. Ave *et al.* (TRACER Collab.), Astrophys. J. **678**, 262 (2008).
13. F. Aharonian *et al.* (HESS Collab.), Phys. Rev. **D75**, 042004 (2007).
14. A.W. Strong *et al.*, Ann. Rev. Nucl. and Part. Sci. **57**, 285 (2007).
15. R.A. Mewaldt *et al.*, Space Science Reviews 99,27(2001).
16. A.A. Abdo *et al.*, Astrophys. J. **698**, 2121 (2009).
17. R. Abbasi *et al.*, Astrophys. J. **718**, L194 (2010).

18. M. Amenomori *et al.*, Astrophys. J. **711**, 119 (2010).
19. J. Chang *et al.* (ATIC Collab.), Nature **456**, 362 (2008).
20. A.A. Abdo *et al.* (Fermi/LAT Collab.), Phys. Rev. Lett. **102**, 181101 (2009); M. Ackermann *et al.*, Phys. Rev. **D82**, 092004 (2010).
21. M. Aguilar *et al.* (AMS-02 Collab.), Phys. Rev. Lett. **113**, 221102 (2014).
22. F. Aharonian *et al.* (HESS Collab.), Phys. Rev. Lett. **101**, 261104 (2008) and Astron. & Astrophys. **508**, 561 (2009).
23. O Adriani *et al.*, Phys. Rev. Lett. **106**, 201101 (2011).
24. L. Accardo *et al.* (AMS-02 Collab.), Phys. Rev. Lett. **113**, 121101 (2014).
25. Y. Shizake *et al.*, Astropart. Phys. **28**, 154 (2007).
26. O. Adriani *et al.* (Pamela Collab.), Nature **458**, 607 (2009); Phys. Rev. Lett. **102**, 051101 (2009).
27. M. Aguilar *et al.*, Phys. Rev. Lett. **110**, 141102 (2013).
28. I.V. Moskalenko and A.W. Strong, Astrophys. J. **493**, 694 (1998).
29. A. Ibarra *et al.*, Int. J. Mod. Phys. **A28**, 1330040 (2013).
30. J.J. Beatty *et al.*, Phys. Rev. Lett. **93**, 24112 (2004).
31. J. Nishimura *et al.*, Adv. Space Research **19**, 767 (1997).
32. D. Gaggero *et al.*, Phys. Rev. Lett. **111**, 021102 (2013).
33. M.A. DuVernois *et al.*, Astrophys. J. **559**, 296 (2001).
34. M. Boezio *et al.*, Astrophys. J. **532**, 653 (2000).
35. A.S. Beach *et al.*, Phys. Rev. Lett. **87**, 271101 (2001).
36. A. Yamamoto *et al.*, Adv. Space Research**42**, 443(2008).
37. Y. Asaoka *et al.*, Phys. Rev. Lett. **88**, 51101 (2002).
38. K. Abe *et al.*, Phys. Rev. Lett. **108**, 081102 (2012).
39. H. Fuke *et al.*, Phys. Rev. Lett. **95**, 081101 (2005).
40. P. Yin *et al.*, Phys. Rev. **D88**, 023001 (2013).
41. R. Bellotti *et al.*, Phys. Rev. **D53**, 35 (1996).
42. R. Bellotti *et al.*, Phys. Rev. **D60**, 052002 (1999).
43. M. Boezio *et al.*, Phys. Rev. **D62**, 032007 (2000); M. Boezio *et al.*, Phys. Rev. **D67**, 072003 (2003).
44. S. Coutu *et al.*, Phys. Rev. **D62**, 032001 (2000).
45. S. Haino *et al.*, Phys. Lett. **B594**, 35 (2004).
46. T. Sanuki *et al.*, Phys. Rev. **D75**, 043005 (2007).
47. T.K. Gaisser, R. Engel, and E. Resconi, *Cosmic Rays and Particle Physics (second edition)*, Cambridge University Press (2016).
48. P. Lipari, Astropart. Phys. **1**, 195 (1993).
49. E. Mocchiutto *et al.*, in *Proc. 28th Int. Cosmic Ray Conf.*, Tsukuba, 1627 (2003). `[http://http://adsabs.harvard.edu/abs/2003ICRC....3.1627M]`.
50. M.P. De Pascale *et al.*, J. Geophys. Res. **98**, 3501 (1993).
51. P.K.F. Grieder, *Cosmic Rays at Earth*, Elsevier Science (2001).
52. J. Kremer *et al.*, Phys. Rev. Lett. **83**, 4241 (1999).
53. S. Haino *et al.* (BESS Collab.), Phys. Lett. **B594**, 35 (2004).
54. P. Archard *et al.* (L3+C Collab.), Phys. Lett. **B598**, 15 (2004).
55. C.G.S. Costa, Astropart. Phys. **16**, 193 (2001).

56. O.C. Allkofer, K. Carstensen, and W.D. Dau, Phys. Lett. **B36**, 425 (1971).
57. B.C. Rastin, J. Phys. **G10**, 1609 (1984).
58. C.A. Ayre *et al.*, J. Phys. **G1**, 584 (1975).
59. H. Jokisch *et al.*, Phys. Rev. **D19**, 1368 (1979).
60. P. Adamson *et al.* (MINOS Collab.), Phys. Rev. **D76**, 052003 (2007).
61. S. Hayakawa, *Cosmic Ray Physics*, Wiley, Interscience, New York (1969).
62. R.R. Daniel and S.A. Stephens, Revs. Geophysics & Space Sci. **12**, 233 (1974).
63. K.P. Beuermann and G. Wibberenz, Can. J. Phys. **46**, S1034 (1968).
64. I.S. Diggory *et al.*, J. Phys. **A7**, 741 (1974).
65. V. Khachatryan *et al.* (CMS Collab.) Phys. Lett. **B692**, 83 (2010).
66. N. Agafonova *et al.* (OPERA Collab.) Eur. Phys. J. **C67**, 25 (2010).
67. D.E. Groom, N.V. Mokhov, and S.I. Striganov, *"Muon stopping-power and range tables,"*Atomic Data and Nuclear Data Tables, **78**, 183 (2001).
68. P. Lipari and T. Stanev, Phys. Rev. **D44**, 3543 (1991).
69. M. Crouch, in *Proc. 20th Int. Cosmic Ray Conf.*, Moscow, **6**, 165 (1987) [http://adsabs.harvard.edu/abs/1987ICRC....6..165C].
70. I.A. Belolaptikov *et al.*, Astropart. Phys. **7**, 263 (1997).
71. J. Babson *et al.*, Phys. Rev. **D42**, 3613 (1990).
72. P. Desiati *et al.*, in *Proc. 28th Int. Cosmic Ray Conf.*, Tsukuba, 1373 (2003) [http://adsabs.harvard.edu/abs/2003ICRC....3.1373D].
73. T. Pradier *et al.* (ANTARES Collab.), arXiv:0805.2545 and 31st ICRC, 7-15 July 2009, Łódź, Poland (paper #0340).
74. S. Aiello *et al.* (NEMO Collab), Astropart. Phys. **66**, 1 (2015).
75. Yu.M. Andreev, V.I. Gurentzov, and I.M. Kogai, in *Proc. 20th Int. Cosmic Ray Conf.*, Moscow, **6**, 200 (1987), [http://adsabs.harvard.edu/abs/1987ICRC....6..200A].
76. M. Aglietta *et al.* (LVD Collab.), Astropart. Phys. **3**, 311 (1995).
77. M. Ambrosio *et al.* (MACRO Collab.), Phys. Rev. **D52**, 3793 (1995).
78. Ch. Berger *et al.* (Frejus Collab.), Phys. Rev. **D40**, 2163 (1989).
79. C. Waltham *et al.*, in *Proc. 27th Int. Cosmic Ray Conf.*, Hamburg, 991 (2001), [http://adsabs.harvard.edu/abs/2001ICRC....3..991W].
80. Y. Ashie *et al.* (SuperKamiokande Collab.), Phys. Rev. **D71**, 112005 (2005).
81. T. Futagami *et al.*, Phys. Rev. Lett. **82**, 5194 (1999).
82. Y. Fukuda *et al.*, Phys. Rev. Lett. **81**, 1562 (1998).
83. F. Reines *et al.*, Phys. Rev. Lett. **15**, 429 (1965).
84. M.M. Boliev *et al.*, in *Proc. 3rd Int. Workshop on Neutrino Telescopes* (ed. Milla Baldo Ceolin), 235 (1991).
85. M. Ambrosio *et al.*, (MACRO) Phys. Lett. **B434**, 451 (1998). The number quoted for MACRO is the average over 90% of the lower hemisphere, $\cos\theta < -0.1$; see F. Ronga *et al.*, hep-ex/9905025.
86. R. Becker-Szendy *et al.*, Phys. Rev. Lett. **69**, 1010 (1992); *Proc. 25th Int. Conf. High-Energy Physics*, Singapore (eds. K.K. Phua and Y. Yamaguchi, World Scientific), 662 1991.
87. S. Hatakeyama *et al.*, Phys. Rev. Lett. **81**, 2016 (1998).

88. Y. Fukuda *et al.*, Phys. Rev. Lett. **82**, 2644 (1999).
89. K. Greisen, Ann. Rev. Nucl. Sci. **10**, 63 (1960).
90. S.P. Swordy *et al.*, Astropart. Phys. **18**, 129 (2002).
91. N.L. Grigorov *et al.*, *Sov. J. Nucl. Phys.* 11, 588. *Proc. 12th Int. Cosmic Ray Conf.*, Hobart, **1**, 1746 and 1752 (1971).
92. K. Asakimori *et al.*, *Proc. 23rd Int. Cosmic Ray Conf.*, Calgary, **2**, 25 (1993); *Proc. 22nd Int. Cosmic Ray Conf.*, Dublin, **2**, 57 and 97 (1991) [http://adsabs.harvard.edu/abs/1991ICRC....2...57A] [http://adsabs.harvard.edu/abs/1991ICRC....2...97A].
93. T.V. Danilova *et al.*, *Proc. 15th Int. Cosmic Ray Conf.*, Plovdiv, **8**, 129 (1977) [http://adsabs.harvard.edu/abs/1977ICRC....8..129D].
94. Yu. A. Fomin *et al.*, *Proc. 22nd Int. Cosmic Ray Conf.*, Dublin, **2**, 85 (1991) [http://adsabs.harvard.edu/abs/1991ICRC....2...85F].
95. M. Amenomori *et al.*, Astrophys. J. **461**, 408 (1996).
96. M. Nagano *et al.*, J. Phys. **G10**, 1295 (1984).
97. F. Arqueros *et al.*, Astron. & Astrophys. **359**, 682 (2000).
98. M.A.K. Glasmacher *et al.*, Astropart. Phys. **10**, 291 (1999).
99. T. Antoni *et al.* (Kascade Collab.), Astropart. Phys. **24**, 1 (2005).
100. M. Amenomori *et al.*, Astrophys. J. **268**, 1165 (2008).
101. W.D. Apel *et al.*, Phys. Rev. Lett. **107**, 171104 (2011).
102. M.G. Aartson *et al.*, (IceCube Collab.) arXiv:1307.3795v1(2013).
103. R. Abbasi *et al.*, (HiRes Collab.), Phys. Rev. Lett. **100**, 101101 (2008).
104. J. Abraham *et al.*, (Auger Collab.), Phys. Rev. Lett. **101**, 061101 (2008).
105. D. Ivanov *et al.*, (Telescope Array Collab.), *Proceedings of Science* (ICRC2015), 349 (2015).
106. F. Fenu *et al.*, (Auger Collab.), *Proceedings of Science* (ICRC2017), 486 (2017).
107. D.J. Bird *et al.*, (Fly's Eye Collab.), Astrophys. J. **424**, 491 (1994).
108. M. Takeda *et al.*, (AGASA Collab.), Astropart. Phys. **19**, 447 (2003).
109. P. Tinyakov *et al.*, (Telescope Array Collab.), *Proceedings of Science* (ICRC2015), 326 (2015).
110. A. Aab *et al.*, (Auger Collab.), *Science* 57, 1266 (2017).
111. V.S. Ptuskin *et al.*, Astron. & Astrophys. **268**, 726 (1993).
112. J.R. Hörandel, Astropart. Phys. **21**, 241 (2004).
113. V.S. Berezinsky and S.I. Grigor'eva, Astron. & Astrophys. **199**, 1 (1988).
114. V. Berezinsky, A. Gazizov, and S. Grigorieva, Phys. Rev. **D74**, 043005 (2006).
115. D. Ikeda *et al.*(TA Collab.), Proceedings of Science(ICRC2017), 515 (2017).
116. J. Bellido *et al.*(Auger Collab.), Proceedings of Science(ICRC2017), 506 (2017).
117. V. de Souza *et al.*(TA and Auger Collabs.), Proceedings of Science(ICRC2017), 522 (2017).
118. K. Greisen, Phys. Rev. Lett. **16**, 748 (1966).
119. G.T. Zatsepin and V.A. Kuz'min, Sov. Phys. JETP Lett. **4**, 78 (1966).
120. D. Allard *et al.*, Astron. & Astrophys. **443**, L29 (2005).
121. M. Aartsen *et al.*, (IceCube Collab.) Science **342**, 1242856 (2013).
122. M. Aartsen *et al.*, (IceCube Collab.) Phys. Rev. Lett. **113**, 101101 (2013).

123. M.G. Aartsen *et al.*(IceCube Collab.), Astrophys. J. **809**, 98 (2015).
124. V.S. Berezinsky and G.T. Zatsepin, Phys. Lett. **B28**, 423 (1969).
125. M.G. Aartsen *et al.*, (IceCube Collab.), Phys. Rev. **D88**, 112008 (2013).
126. A. Aab *et al.*, (Auger Collab.), Phys. Rev. **D91**, 092008 (2015).
127. I. Kravchenko *et al.*(RICE Collab.), Phys. Rev. **D73**, 082002 (2006);
I. Kravchenko *et al.*(RICE collab.), Phys. Rev. **D85**, 062004 (2012).
128. P. Gorham *et al.*, (ANITA Collab.), Phys. Rev. **D82**, 022004 (2010);
P. Gorham *et al.*, (ANITA Collab.), Phys. Rev. **D85**, 049901 (2012).
129. R. Engel, D. Seckel, and T. Stanev, Phys. Rev. **D64**, 09310 (2001).
130. E. Waxman and J. Bahcall, Phys. Rev. **D59**, 023002 (1999).
131. R.U. Abbasi *et al.*, (HiRes Collab.), Astropart. Phys. **32**, 53 (2009).